Ultrasonics 131 (2023) 106951

Contents lists available at ScienceDirect

Ultrasonics

journal homepage: www.elsevier.com/locate/ultras

Ultrasonic bandgaps in viscoelastic 1D-periodic media: Mechanical modeling and experimental validation

Max Gattin [a], Nicolas Bochud [a,*], Giuseppe Rosi [a], Quentin Grossman [b], Davide Ruffoni [b], Salah Naili [a]

[a] Univ Paris Est Creteil, Univ Gustave Eiffel, CNRS, UMR 8208, MSME, F-94010, Créteil, France
[b] Mechanics of Biological and Bioinspired Materials Laboratory, Department of Aerospace and Mechanical Engineering, University of Liège, Quartier Polytech 1, Allée de la Découverte, B-4000 Liège, Belgium

ARTICLE INFO

Keywords:
Bloch–Floquet analysis
Transfer matrix formalism
Periodic media
Viscoelasticity
Bandgaps
Multi-material additive manufacturing

ABSTRACT

Multi-material additive manufacturing is receiving increasing attention in the field of acoustics, in particular towards the design of micro-architectured periodic media used to achieve programmable ultrasonic responses. To unravel the effect of the material properties and spatial arrangement of the printed constituents, there is an unmet need in developing wave propagation models for prediction and optimization purposes. In this study, we propose to investigate the transmission of longitudinal ultrasound waves through 1D-periodic biphasic media, whose constituent materials are viscoelastic. To this end, Bloch–Floquet analysis is applied in the frame of viscoelasticity, with the aim of disentangling the relative contributions of viscoelasticity and periodicity on ultrasound signatures, such as dispersion, attenuation, and bandgaps localization. The impact of the finite size nature of these structures is then assessed by using a modeling approach based on the transfer matrix formalism. Finally, the modeling outcomes, *i.e.*, frequency-dependent phase velocity and attenuation, are confronted with experiments conducted on 3D-printed samples, which exhibit a 1D periodicity at length-scales of a few hundreds of micrometers. Altogether, the obtained results shed light on the modeling characteristics to be considered when predicting the complex acoustic behavior of periodic media in the ultrasonic regime.

1. Introduction

Additive manufacturing (AM), also referred to as 3D printing, has experienced a wide dissemination in the field of acoustics over the past few years, in particular towards the design of structures with complex geometries and/or material distributions used to achieve specific acoustic responses [1]. This concerns for instance the development of biomedical applications, such as the prototyping of tissue-mimicking phantoms for ultrasound imaging system assessment [2,3] and the conception of acoustic lenses to correct transcranial focused ultrasound aberrations [4,5]. Likewise, 3D printing also has proven to be useful to design periodic media, such as phononic crystals or metamaterials [6].

In this specific context, most experimental validations conducted so far have focused on a rather low frequency regime (from about 10 to 100 kHz), with manifold applications ranging from underwater acoustics to vibration mitigation and sound attenuation, as well as elastic wave control [7–10]. In contrast, analogous experimental realizations in the ultrasonic regime have scarcely been reported in the literature [11], especially because of manufacturing constraints. Indeed, Bragg interferences only appear for media whose periodic characteristic length is of the same order of magnitude than the wavelength of interest, *i.e.*, several hundreds of micrometers for the MHz regime, which is still difficult to achieve with most current 3D printing technologies. Nevertheless, these length scales correspond to the size of the microstructures involved in biological materials, which show well defined architectures and structural patterns at several hundreds of micrometers [12,13]. Likewise, these length scales are also relevant for orthopedic applications, such as scaffolds intended for tissue engineering and bone repair purposes [14,15] or the so-called meta-biomaterials [16], which overall motivate the investigation of wave propagation across periodic media in the ultrasonic regime.

Before the recent democratization of AM, periodic media already have been investigated in the MHz regime, either by using liquid-filled drilled metallic plates [17] or by juxtaposing thin aluminum and polyethylene plates to obtain periodic multilayers [18,19]. Later, some 3D printing developments also have been proven feasible to manufacture more sophisticated periodic lattices with characteristic length compatible with the MHz regime, such as direct laser metal sintering [20], robocasting for the fabrication of ceramic micro-rods [21], and high

* Corresponding author.
E-mail address: nicolas.bochud@u-pec.fr (N. Bochud).

https://doi.org/10.1016/j.ultras.2023.106951
Received 28 October 2022; Received in revised form 29 December 2022; Accepted 6 February 2023
Available online 10 February 2023

resolution stereolithography [22,23], which is dedicated to polymers. While the latter techniques have been specifically used to design air- or water-filled architectures only, some others, like inkjet-based AM, also allow for the multi-material fabrication of structures, whose solid constituent materials exhibit dissimilar properties. Notwithstanding, such multiphasic periodic composite materials have been mainly studied in the quasi-static regime so far [24–26], and the possibility to take advantage of this technique to achieve ultrasonic phononic media still remains to be explored.

In this study, we propose to investigate the transmission of longitudinal ultrasound waves propagating in normal incidence across 1D-periodic media made of two dissimilar photopolymers (*i.e*, a rigid glassy polymer and a compliant rubbery polymer), which were obtained using multi-material polyjet AM. The investigated configuration was intentionally chosen to be as simple as possible, in order to assess the feasibility of making use of such a 3D printing technology to design multi-material periodic samples and achieve programmable ultrasonic responses in a laboratory-controlled environment. Overall, the proposed approach was motivated by two main objectives. As previous works by our group showed that these photopolymer materials display viscoelastic properties in the MHz regime [27,28], here we first seek to disentangle the relative contributions of viscoelastic constituent materials and Bragg scattering on the apparent ultrasonic behavior of 1D-periodic media using Bloch–Floquet analysis. Second, since the high ultrasonic attenuation associated with such materials fundamentally limits the dimensions of the samples for practical applications, a transfer matrix formalism is implemented to assess the validity of the Bloch–Floquet analysis for 1D-periodic media that consists of a finite number of unit cell repetitions. As a by-product, both modeling approaches are subsequently used to infer the ultrasonic responses of several 1D-periodic media with different unit cell sizes, which are in turn confronted to ultrasound measurements performed on AM samples. Altogether, the reported results suggest that a modeling approach, which accounts for the viscoelastic and finite size nature of the samples, could be further used as a valuable guide towards the design of complex periodic media with programmable acoustic responses.

2. Mechanical modeling

2.1. Bloch–Floquet analysis in the frame of viscoelasticity

Let us consider an infinite biphasic medium that consists of a periodically replicated unit cell of thickness d. As depicted in Fig. 1, the unit cell itself is made of two constituent material layers m, each one with given thickness d_m, mass density ρ_m, and wave number $k_m(\omega)$, where $m \in \{A, B\}$ and ω is the angular frequency.

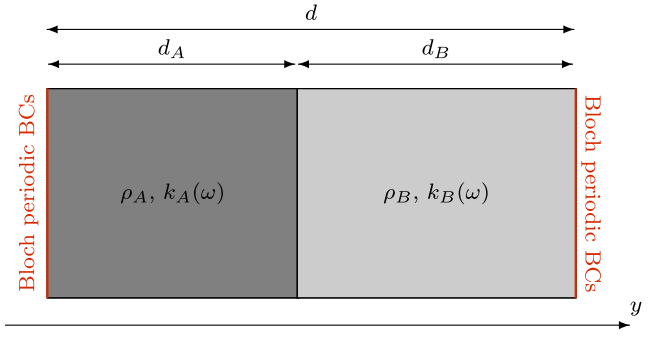

Fig. 1. Schematic representation of the 1D unit cell used in the Bloch–Floquet analysis, which is made of two constituent material layers m, with given thickness d_m, mass density ρ_m, and wave number $k_m(\omega)$, where $m \in \{A, B\}$.

In the case of a 1D harmonic plane wave propagating in such an infinite medium along the y-direction (*i.e.*, perpendicular to the layers), the displacement field can be written as $u(y,\omega) = (A_0 \exp(-jk(\omega)y) + B_0 \exp(jk(\omega)y)) \exp(j\omega t)$, with j being the unit imaginary number and $k(\omega)$ being the Bloch wave number. By applying Bloch periodic boundary conditions (BCs), *i.e.*, $u(y+d,\omega) = \exp(-jk(\omega)d)u(y,\omega)$, it can be shown that the Bloch wave number $k(\omega)$ satisfies the dispersion relation [29,30]:

$$\cos(k(\omega)d) = \cos(k_A(\omega)d_A)\cos(k_B(\omega)d_B) - \frac{1}{2}\left(\frac{Z_A(\omega)}{Z_B(\omega)} + \frac{Z_B(\omega)}{Z_A(\omega)}\right)\sin(k_A(\omega)d_A)\sin(k_B(\omega)d_B)\,, \quad (1)$$

where $Z_m = \rho_m\omega/k_m(\omega)$ is the complex acoustic impedance of each constituent material m. Two specific cases are considered in the following: (1) A pure elastic case, where the wave numbers of the constituent materials $k_m(\omega)$ are considered as purely real, with constant phase velocity, and (2) a viscoelastic case, where the wave numbers $k_m(\omega)$ are complex and can thus be written as $k_m(\omega) = \omega/v_m(\omega) - j\alpha_m(\omega)$, with $v_m(\omega)$ and $\alpha_m(\omega)$ being the phase velocity and attenuation, respectively.

Without loss of generality, for the latter case we assume that the viscoelastic behavior of the constituent materials m can be modeled using an attenuation $\alpha_m(\omega)$ that is governed by a frequency power-law [31]. This choice is motivated by the experimental evidence that many lossy materials, among which photopolymers, satisfy this assumption in the ultrasonic regime [28]. Hence,

$$\alpha_m(\omega) = \alpha_{0m} + (\alpha_{cm} - \alpha_{0m})\left(\frac{\omega}{\omega_c}\right)^{y_m}\,, \quad (2)$$

where $\omega = 2\pi f$ is the angular frequency and y_m is a dimensionless exponent, which usually ranges from 0 to 2. Note that the original expression introduced by Szabo and Wu [32] has here been normalized with respect to an arbitrary angular frequency $\omega_c = 2\pi f_c$, so that the model parameters α_{0m} and α_{cm} respectively denote the attenuations at the angular frequency $\omega = 0$ and $\omega = \omega_c$ [28]. Causality via Kramers–Kronig relation implies that the frequency dependence of the phase velocity $v_m(\omega)$ and of the attenuation $\alpha_m(\omega)$ are not independent [33]. Therefore, according to Eq. (2), it can be shown that the frequency-dependent phase velocity $v_m(\omega)$ must take the form [32]

$$v_m(\omega) = \left(\frac{1}{v_{cm}} + (\alpha_{cm} - \alpha_{0m})\tan(y_m\pi/2)\left(\left(\frac{\omega}{\omega_c}\right)^{y_m}\omega^{-1} - \omega_c^{-1}\right)\right)^{-1}\,, \quad (3)$$

where v_{cm} is the phase velocity at the angular frequency ω_c. It is noteworthy that this model exhibits a mathematical singularity for $y_m = 1$. For such a case, modified expressions for the phase velocity and attenuation can be found in Szabo and Wu [32].

Under these considerations, the phase velocity $v_m(\omega)$ and attenuation $\alpha_m(\omega)$ used as input data to feed Eq. (1) for the viscoelastic case are given in Fig. 2 (continuous red lines) for two constituent materials m, whose mechanical properties were chosen according to Aghaei et al. [27], in order to mimic those of a rigid glassy polymer ($m = A$) and an elastomeric polymer ($m = B$). Likewise, their respective elastic counterparts (*i.e.*, $v_m(\omega) = v_{cm}$ and $\alpha_m(\omega) = 0$) used as input data to feed Eq. (1) for the elastic case are given for comparison in Fig. 2 (dotted black lines).

For the infinite 1D-periodic medium made of these two constituent materials m, the resulting complex dispersion relation (recall Eq. (1)) is depicted in Fig. 3 for both the pure elastic and viscoelastic cases. One should first keep in mind that the solution is shown in the first Brillouin zone only. Indeed, the full solution of Eq. (1) for the product $k(\omega)d$ is 2π-periodic and symmetric from π to 2π in the real plane. Moreover, in the imaginary plane, the solution is symmetric with respect to 0. As can be observed, in the case of purely elastic constituent materials (dotted black lines), one can identify two different frequency regimes: A propagative regime, where the Bloch wave number $k(\omega)$ evolves in the purely real plane, and an evanescent regime, where the Bloch wave number $k(\omega)$ evolves in the purely imaginary plane only, which results in strongly attenuated frequency bands called bandgaps (light gray areas around 1.5 and 3 MHz). In addition, a remarkable property of elastic periodic media is the presence of zero group velocity (ZGV)

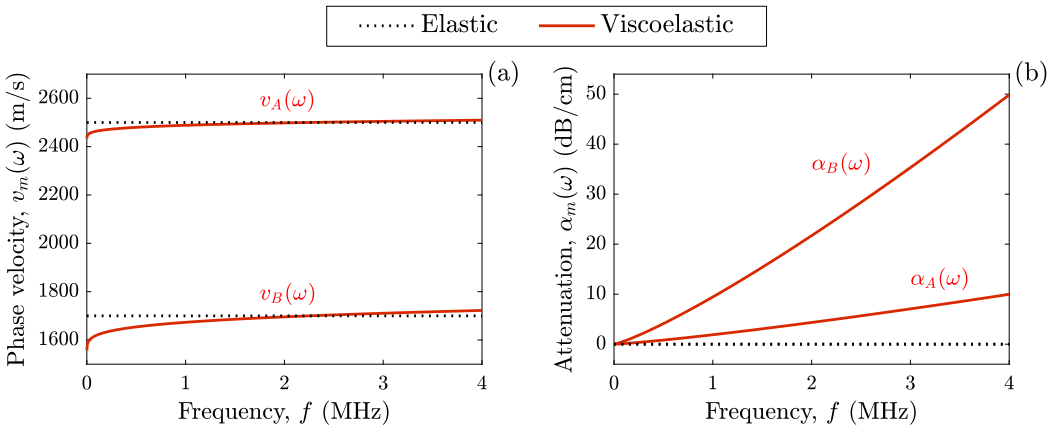

Fig. 2. Ultrasound characteristics of the two constituent materials m, with $m \in \{A, B\}$, for the purely elastic (dotted black lines) and viscoelastic (continuous red lines) cases: (a) Phase velocity $v_m(\omega)$ and (b) Attenuation $\alpha_m(\omega)$. These were calculated using the following model parameters: $v_{cA} = 2500$ m/s, $\alpha_{cA} = 5$ dB/cm, $\alpha_{0A} = 0$ dB/cm, $y_A = 1.2$, and $v_{cB} = 1700$ m/s, $\alpha_{cB} = 25$ dB/cm, $\alpha_{0B} = 0$ dB/cm, $y_B = 1.2$.

modes, that is $\partial\omega/\partial k(\omega) = 0$, at the crossing points of the cutoff frequencies of the bandgaps (*i.e.*, upper and lower limits of the light gray areas) and the limits of the Brillouin zones. Conversely, in the case of viscoelastic constituent materials (continuous red lines), the Bloch wave number $k(\omega)$ concurrently evolves in both the real and imaginary planes, no matter the frequency. Indeed, outside the bandgaps, its imaginary part, denoted by $\Im(k(\omega))$, slowly increases with frequency while its real part, denoted by $\Re(k(\omega))$, is slightly modified compared to the pure elastic case, owing to the dispersion induced by the viscoelasticity of the constituent materials. However, inside the bandgaps, while its imaginary part $\Im(k(\omega))$ increases similarly to the pure elastic case, its real part $\Re(k(\omega))$ does not remain constant, losing therefore the ZGV property at the cutoff frequencies.

Alternatively, the acoustic behavior of the wave motion associated with the infinite 1D-periodic medium can also be interpreted based on apparent ultrasound characteristics, *i.e.*, using the phase velocity $v(\omega)$ and attenuation $\alpha(\omega)$. Indeed, by considering propagation towards the positive y-direction and thus keeping only solutions with positive phase and group velocities (across the multiple Brillouin zones), the apparent phase velocity and attenuation can be deduced from the Bloch wave number $k(\omega)$ as $v(\omega) = \omega/\Re(k(\omega))$ and $\alpha(\omega) = -\Im(k(\omega))$, respectively. In fact, the extraction of such apparent ultrasound characteristics consists in considering the wave motion of the periodic medium as that of an apparent homogeneous one [34]. Thereby, all interferences due to the presence of the scatterers (*i.e.*, interfaces between two phases) are expressed in terms of apparent dispersion and attenuation of a single wave rather than the stacking of multiple scattered waves.

The apparent phase velocity $v(\omega)$ and attenuation $\alpha(\omega)$ are depicted in Fig. 4 for the pure elastic (dotted black lines) and viscoelastic (continuous red lines) cases. In addition, the effective viscoelastic case (dashed blue lines), which is based on the long-wavelength, low-frequency approximation [35], is also presented for comparison (see Supplementary Material 1). As can be observed, the variations of the phase velocity $v(\omega)$ and attenuation $\alpha(\omega)$ for the viscoelastic case result from two concurrent contributions: (1) the slow increase of these apparent ultrasound characteristics with frequency is mostly related to the viscoelastic behavior of the constituent materials, as it is present in the effective case but not in the elastic one; and (2) their sudden variations in the bandgaps result from periodicity effects (Bragg scattering), as they are present in the elastic case but not in the effective one. Altogether, these observations also evidence that a coupling takes place between viscoelasticity and periodicity effects, as the solution

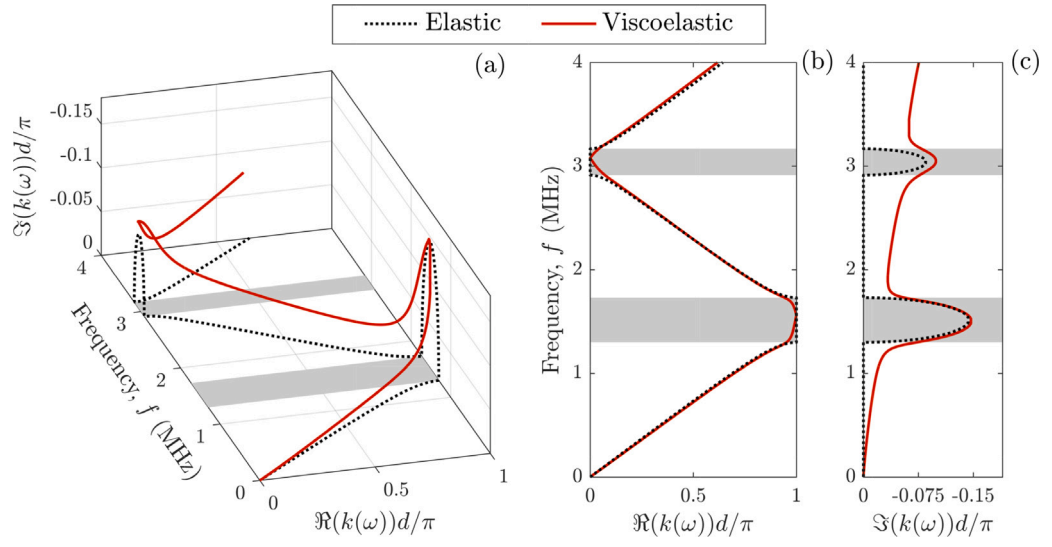

Fig. 3. Normalized dispersion diagram for an infinite 1D-periodic medium, displayed for the pure elastic (dotted black lines) and viscoelastic (continuous red lines) cases: (a) Complex Bloch wave number $k(\omega)$ as a function of the frequency f in the first Brillouin zone; (b) Projection of $k(\omega)$ on the real plane; and (c) Projection of $k(\omega)$ on the imaginary plane. The light gray areas display the positions of the bandgaps for the elastic case. The solutions of Eq. (1) were calculated using the input data from Fig. 2, together with the following thicknesses and mass densities: $d_A = d_B = d/2 = 667$ µm, $\rho_A = 1200$ kg/m^3, and $\rho_B = 1100$ kg/m^3.

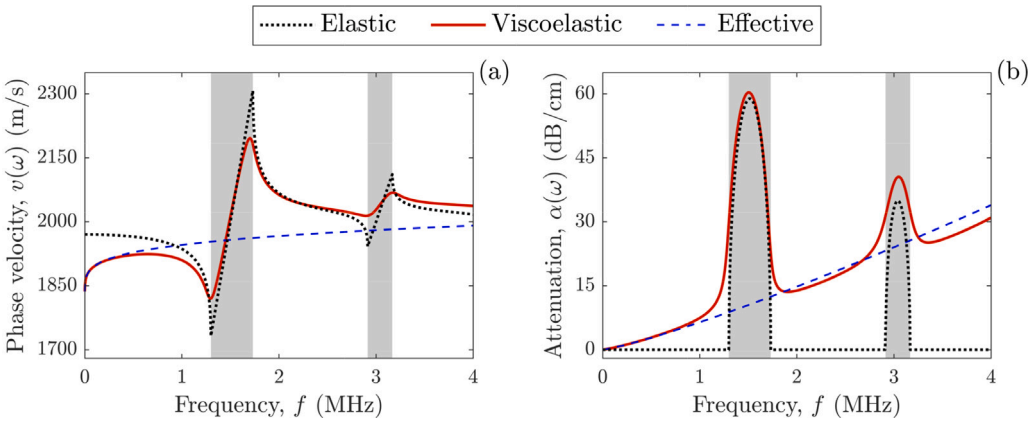

Fig. 4. Apparent ultrasound characteristics extracted from the normalized dispersion diagram depicted in Fig. 3 for an infinite 1D-periodic medium, for the purely elastic (dotted black lines) and viscoelastic (continuous red lines) cases: (a) Phase velocity $v(\omega)$ and (b) Attenuation $\alpha(\omega)$. The light gray areas display the positions of the bandgaps for the elastic case. The effective viscoelastic case (dashed blue lines) is also provided for comparison.

for the viscoelastic case is not a mere addition of the contributions of the elastic and the effective cases. Indeed, this coupling leads to a smoothing of the phase velocity in comparison with the elastic case and therefore to a vanishing of the ZGV property at the cutoff frequencies (see Fig. 4(a)). Likewise, it also causes a significant enlargement, as well as a slight frequency shift, of the bandgaps (see Fig. 4(b)).

2.2. Assessment of the finite size nature of the samples

While Bloch–Floquet analysis provides an efficient way to model the (visco)elastic behavior of periodic media, such modeling approach is valid only when considering an infinite number of periodic spatial repetitions N of the unit cell (*i.e.*, $N \to \infty$). Since samples are of finite nature in practice, here we aim at assessing the impact of a finite size periodic medium on the retrieved apparent ultrasound characteristics (*e.g.*, phase velocity, attenuation, complex wave number), in order to provide a quantitative evaluation of the validity range of Bloch–Floquet analysis. To this end, we propose to make use of the transfer matrix formalism, which allows describing the wave propagation in successive piecewise linear homogeneous, viscoelastic media [27,36]. Let us first describe the wave propagation across a single unit cell, as depicted in Fig. 5.

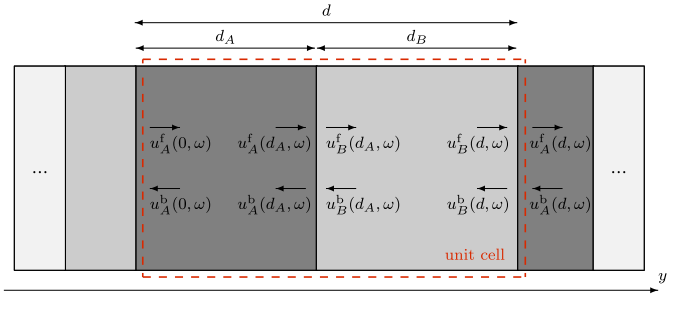

Fig. 5. Schematic representation of the transfer matrix formalism for a wave propagating across a single unit cell.

A harmonic solution for the displacement can be stated in the frequency domain for each material m, with $m \in \{A, B\}$, as

$$u_m(y,\omega) = u_m^{\mathrm{f}}(y,\omega) + u_m^{\mathrm{b}}(y,\omega) \ , \tag{4}$$

where $u_m^{\mathrm{f}}(y,\omega)$ and $u_m^{\mathrm{b}}(y,\omega)$ stand for the forward- and backward-propagating components of the displacement in each material m, respectively.

In the case of a perfectly bonded interface between the two materials, the transmission conditions imply the continuity of displacement and stress across this interface. Thereby, the transition from material A to B (and vice versa) can be expressed as in Cretu and Nita [37],

$$\boldsymbol{u}_B(d_A,\omega) = \boldsymbol{D}_{AB}(\omega)\boldsymbol{u}_A(d_A,\omega) \ , \tag{5a}$$

$$\boldsymbol{u}_A(d,\omega) = \boldsymbol{D}_{BA}(\omega)\boldsymbol{u}_B(d,\omega) \ , \tag{5b}$$

where $\boldsymbol{u}_m(y,\omega) = [u_m^{\mathrm{f}}(y,\omega), u_m^{\mathrm{b}}(y,\omega)]^T$ is the state vector of material m, with T being the transpose operator. The (2×2)-discontinuity matrix $\boldsymbol{D}_{m\bar{m}}(\omega)$, which only depends on the complex acoustic impedance of the two materials being in contact, can be defined as

$$\boldsymbol{D}_{m\bar{m}}(\omega) = \frac{1}{2}\begin{pmatrix} 1+\dfrac{Z_m}{Z_{\bar{m}}} & 1-\dfrac{Z_m}{Z_{\bar{m}}} \\ 1-\dfrac{Z_m}{Z_{\bar{m}}} & 1+\dfrac{Z_m}{Z_{\bar{m}}} \end{pmatrix}, \quad \text{with} \quad \bar{m} = \begin{cases} B, & \text{if } m = A \\ A, & \text{if } m = B \end{cases} . \tag{6}$$

In the same way, considering a harmonic wave propagating within the same homogeneous material m, its transformed displacement can be expressed by means of the (2×2)-propagation matrix $\boldsymbol{P}_m(\omega)$ for either A or B as

$$\boldsymbol{u}_A(d_A,\omega) = \boldsymbol{P}_A(\omega)\boldsymbol{u}_A(0,\omega) \ , \tag{7a}$$

$$\boldsymbol{u}_B(d,\omega) = \boldsymbol{P}_B(\omega)\boldsymbol{u}_B(d_A,\omega) \ , \tag{7b}$$

with

$$\boldsymbol{P}_m(\omega) = \begin{pmatrix} \exp(-jk_m(\omega)d_m) & 0 \\ 0 & \exp(jk_m(\omega)d_m) \end{pmatrix} . \tag{8}$$

The relation between the input and output state vectors for a single layer of material m can therefore be expressed by means of the so-called transfer matrix as $\boldsymbol{T}_m(\omega) = \boldsymbol{D}_{m\bar{m}}(\omega)\boldsymbol{P}_m(\omega)$. This allows us to further define the transfer matrix of the unit cell, denoted by $\boldsymbol{T}_{uc}(\omega)$, which relates the state vectors $\boldsymbol{u}_A(d,\omega)$ and $\boldsymbol{u}_A(0,\omega)$, as

$$\boldsymbol{T}_{uc}(\omega) = \boldsymbol{T}_B(\omega)\boldsymbol{T}_A(\omega) \ . \tag{9}$$

Thereby, the total transfer matrix of a 1D-periodic medium made of N unit cells, denoted by $\boldsymbol{T}_N(\omega)$, can easily be obtained by raising the transfer matrix of a single unit cell to the power N as

$$\boldsymbol{T}_N(\omega) = \left(\boldsymbol{T}_{uc}(\omega)\right)^N \ , \tag{10}$$

which accounts for all the reflections, transmissions, losses, and periodicity effects of the wave propagating across the 1D-periodic medium. Applying the Sommerfeld radiation condition at the right boundary of the medium, *i.e.*, $u_A^{\mathrm{b}}(Nd,\omega) = 0$, allows recovering the transfer function $H_N(\omega)$, which relates the transmitted wave $u_A^{\mathrm{f}}(Nd,\omega)$ to the

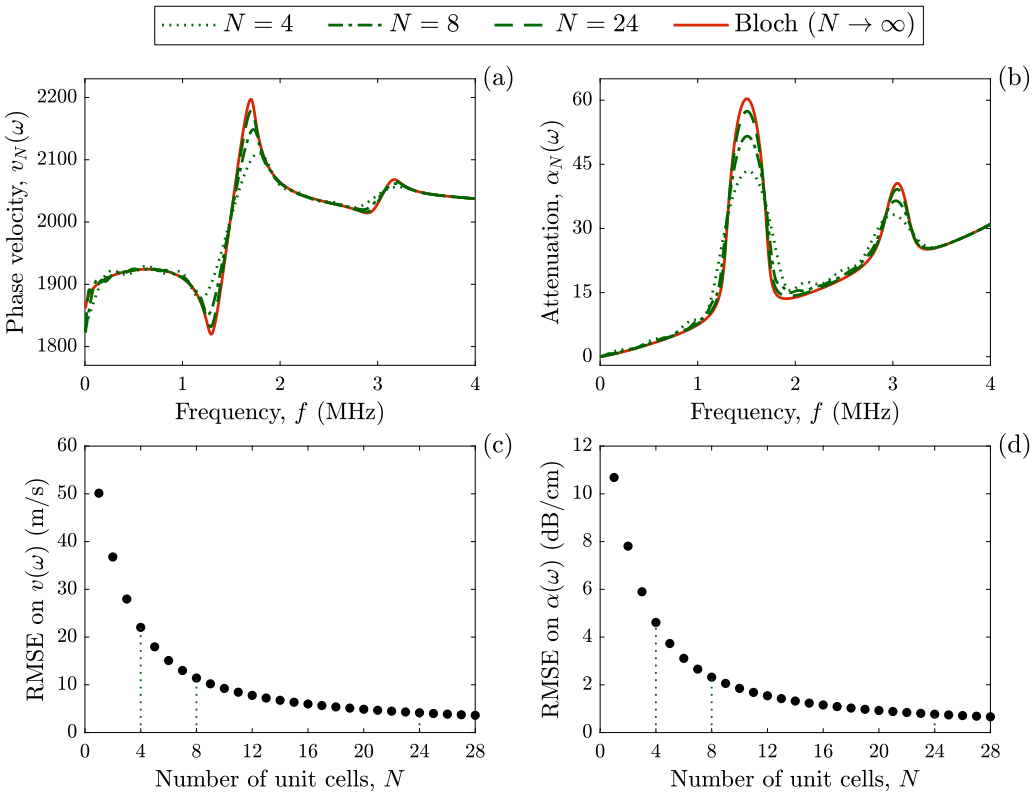

Fig. 6. Impact of the finite size nature of a 1D-periodic medium on the apparent ultrasound characteristics modeled using the transfer matrix formalism: (a) Phase velocity $v_N(\omega)$ and (b) Attenuation $\alpha_N(\omega)$, displayed for three different values of the number of unit cells N (dotted and dashed green lines) and compared to the infinite case (continuous red lines, taken from Fig. 4); (c) RMSE on the phase velocity and (d) RMSE on the attenuation, as a function of the number of unit cells N.

incident wave $u_A^{\mathrm{f}}(0,\omega)$ as

$$H_N(\omega) = \frac{u_A^{\mathrm{f}}(Nd,\omega)}{u_A^{\mathrm{f}}(0,\omega)} = \frac{\det\left(\boldsymbol{T}_N(\omega)\right)}{T_{22}(\omega)}\ , \tag{11}$$

where $T_{22}(\omega)$ is the lower right component of the (2×2)-matrix $\boldsymbol{T}_N(\omega)$. Moreover, it can be shown that the determinant of the total transfer matrix $\det\left(\boldsymbol{T}_N(\omega)\right) = 1$ for such linear, and therefore reciprocal system [38]. A natural manner to make the comparison with Bloch–Floquet analysis easier is to extract the apparent phase velocity and attenuation of the periodic medium by interpreting the multiple scattering as the dispersion and attenuation of an apparent homogeneous medium of thickness $N\times d$. Therefore, by modeling the transfer function as a single forward propagating plane wave, *i.e.*, $H_N(\omega) = \exp(-jk_N(\omega)Nd)$, with $k_N(\omega) = \omega/v_N(\omega) - j\alpha_N(\omega)$, one can deduce expressions for the apparent phase velocity and attenuation of the wave propagating across the finite medium as

$$v_N(\omega) = -\frac{\omega Nd}{\arg(H_N(\omega))}\ , \tag{12a}$$

$$\alpha_N(\omega) = -\frac{1}{Nd}\ln\left(\left|H_N(\omega)\right|\right)\ , \tag{12b}$$

where arg and ln denote the argument and natural logarithm of the quantity.

The apparent phase velocity $v_N(\omega)$ and attenuation $\alpha_N(\omega)$ are depicted in Fig. 6(a)–(b) for different values of N and compared to the solutions ($N\to\infty$) obtained using Bloch–Floquet analysis (recall Fig. 4). In addition, a more quantitative insight into the differences between both modeling approaches is depicted in Fig. 6(c)–(d), which shows the root-mean-squared errors (RMSE) for both apparent ultrasound characteristics over the considered frequency range as a function of the number of unit cell repetitions N. As can be observed, for both the apparent phase velocity and attenuation, the solution obtained with the transfer matrix formalism (dotted and dashed green lines) converges towards Bloch–Floquet solution (continuous red lines) when the number of considered unit cells N increases. This means that, from a sufficiently high number of unit cells, Bloch Floquet analysis is in reasonable agreement with the transfer matrix formalism. However, for lower values of N, it fails in properly capturing the variations in the bandgaps and the oscillations due to Fabry–Perot interferences in the low frequency regime (< 1 MHz).

3. Material and methods

3.1. Measurement method

In this study, the ultrasound measurement of 1D-periodic media was performed based on the so-called insertion-substitution method [39]. The latter first consists in measuring a longitudinal wave transmitted in normal incidence through a water-immersed sample (see Fig. 7), denoted by $u_1(t)$, where t is the time, and then in removing the sample without moving the transducers to measure a reference wave transmitted through water only, denoted by $u_0(t)$. The proposed approach relies on several considerations [40,41]. First, it has the advantage of removing the impact of the frequency response of the transducers. Second, given the highly attenuating nature of the investigated samples, the attenuation in water can be neglected. Third, the distance between the emitting transducer and the sample is set to be large compared to the size of the transducer, so that the acoustical field close to the sample can be modeled under the plane wave assumption. Fourth, making use of a reference measurement $u_0(t)$ naturally cancels out the diffraction effects common to both measurements (*i.e.*, $u_0(t)$ and $u_1(t)$), thereby leaving only the eventual additional diffraction due to the presence of the sample in the first measurement $u_1(t)$, which is here considered as negligible.

Under those considerations, the recorded signals $u_i(t)$, with $i = 0, 1$, can be written in the Fourier domain as $U_i(\omega) = A_i(\omega)\exp(j\varphi_i(\omega))$,

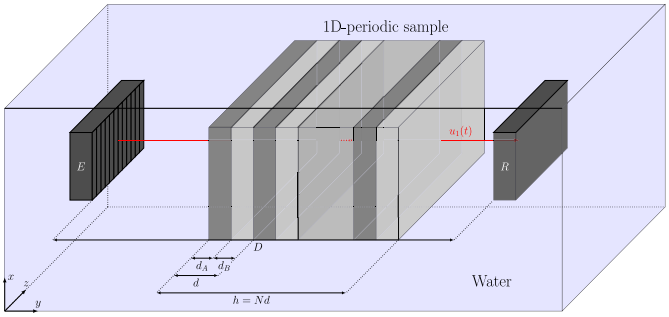

Fig. 7. Schematic representation of the measurements method, where the 1D-periodic sample is placed in water between the emitting (E) and receiving (R) transducers.

where $A_i(\omega)$ and $\varphi_i(\omega)$ represent their amplitude and phase spectra, respectively. Modeling these signals as the result of a single forward plane wave propagating between the two transducers leads to

$$U_0(\omega) = A_0(\omega)\exp(j\varphi_0(\omega)) = A_0(\omega)\exp(-jk_w D)\ , \tag{13a}$$

$$U_1(\omega) = A_1(\omega)\exp(j\varphi_1(\omega)) = T_{\text{tot}}(\omega)A_0(\omega)\exp(-jk_w(D-h))H(\omega)\ , \tag{13b}$$

where D is the distance between both transducers, and $k_w = \omega/c_w$ is the wave number in water, with c_w being the wave celerity in water. Without loss of generality, the transfer function that describes the wave propagation across the 1D-periodic sample only is here denoted by $H(\omega)$. The total transmission coefficient $T_{\text{tot}}(\omega)$, which accounts for both the water-sample and sample-water interfaces, is given by

$$T_{\text{tot}}(\omega) = \frac{4Z(\omega)Z_w}{\left(Z(\omega)+Z_w\right)^2}\ , \tag{14}$$

where $Z(\omega) = \rho v(\omega)$ and $Z_w = \rho_w c_w$ are the acoustic impedances of the sample and of the immersion medium, with ρ and ρ_w being their respective mass densities. Given that it is reasonable to assume the imaginary part of $Z(\omega)$ to be negligible, the transfer function $H(\omega)$ can be derived from Eqs. (13a)–(13b) as

$$H(\omega) = \frac{A_1(\omega)}{A_0(\omega)T_{\text{tot}}(\omega)}\exp\left(j\left(\Delta\varphi(\omega) - \frac{\omega h}{c_w}\right)\right)\ , \tag{15}$$

where $\Delta\varphi(\omega) = \varphi_1(\omega) - \varphi_0(\omega)$. Further assuming that the transfer function can be expressed as $H(\omega) = \exp(-jk(\omega)h)$ allows recovering the apparent phase velocity $v(\omega)$ and attenuation $\alpha(\omega)$ as

$$v(\omega) = -\frac{\omega h}{\arg(H(\omega))}\ , \tag{16a}$$

$$\alpha(\omega) = -\frac{1}{h}\ln(|H(\omega)|)\ . \tag{16b}$$

It should be noted that such representation turns out to be similar to that proposed in the modeling approaches (recall Sections 2.1 and 2.2), as it consists in measuring the ultrasound characteristics of the 1D-periodic medium as those of an apparent homogeneous sample.

3.2. Additively manufactured samples

Additive manufacturing of the samples was carried out using a commercial multi-material 3D printer (Object 260, Stratasys, US), which is based on polyjet technology. The latter applies a layer-by-layer method where multiple streams of UV-curable photopolymers are jetted through printing nozzles onto a building tray [24]. Two dissimilar photopolymers have been used, a rigid glassy polymer (commercial name VeroWhitePlus, VW^+) and an elastomeric polymer (commercial name TangoBlackPlus, TB^+), to ensure a sufficient acoustic contrast between the two phases. Five samples were investigated here. Three 1D-periodic samples were designed as multiple repetitions N of a unit cell, which consists in a VW^+ and a TB^+ layer of equal thickness, resulting in a volume fraction of 50% for each constituent material. In addition, two homogeneous samples, *i.e.,* one for each constituent material, were 3D-printed to serve as a reference for model calibration purposes. Their overall nominal dimensions were set to $50.796\times8.127\times25.400$ mm^3, printed with a voxel size of $42.33\times84.66\times31.75$ µm^3, along the x, y, and z, respectively (see Fig. 7). For the three periodic samples, the unit cell repetitions were along the y-direction and set to $N = 8$, $N = 12$ and $N = 24$, resulting in a nominal unit cell thickness d of 1.016, 0.677, and 0.339 mm, respectively.

The sample dimensions in the xz-plane were chosen according to the characteristics of the ultrasonic probes, *i.e.*, so that they cover the entire emission and reception area of the transducers (recall Fig. 7). Likewise, the nominal thickness of the samples along the y-axis, denoted by h, was chosen based on two criteria. First, it had to be thin enough to allow for a sufficient wave transmission across the sample, thereby ensuring a reasonable signal to noise ratio (SNR) despite attenuation. Second, it had to be thick enough so that, for the 1D-periodic samples, the number of unit cell repetitions N allowed the onset of periodicity effects. To account for the measurement uncertainties, the dimensions and mass of the samples were manually measured eight times by the same operator, using a digital caliper (±0.01 mm) and an electronic precision balance (±1 mg), respectively.

3.3. Experimental setup

All measurements were performed using two multielement probes (Imasonic SAS, France) driven by a programmable multi-channel electronics (Advanced OEM Solutions, WestChester, USA). The two linear transducer arrays consisted of 32 elements each, where each element had a width and a height of 0.5 and 12 mm, respectively, leading to a total transmission area of 16×12 mm^2. The transducers operated at a central frequency $f_c = 2.25$ MHz (−18 dB frequency bandwidth ranging from 1.15 to 3.15 MHz) and the pitch of the arrays was 0.5 mm. Measurements were carried out using a plane wave imaging mode, by simultaneously launching a pulse on all elements of the emitting array. The transmitted signals were recorded on the receiving array during 150 µs (from 100 to 250 µs after the emission), digitized with a sample frequency $f_s = 100$ MHz, and quantized with a 12-bit resolution. It should be noted that the wavelength in water in this frequency regime is small compared to the dimensions of the emitting array, which implies a high directivity factor of the source and a weak geometric attenuation that further support the assumption of negligible diffraction [28].

Prior to the measurements, optimal azimuthal alignment between the two transducers and the sample was concurrently obtained by minimizing the time-of-flight difference of the signals received on the leftmost and rightmost elements of both the emitting and receiving arrays. Likewise, optimal vertical alignment was achieved by maximizing the SNR of the transmitted signals. Each measurement was repeated eight times to account for the statistical dispersion of the frequency-dependent phase difference (*i.e.*, $\Delta\varphi(\omega)$) and amplitude ratio (*i.e.*, $A_0(\omega)/A_1(\omega)$). The temperature during the measurements was 25 °C (measured using a Zacro LCD digital thermometer, with a resolution of ±0.5 °C), so that the water celerity could be estimated using Marczak's polynomial model [42].

To extract ultrasound characteristics, *i.e.*, the phase velocity $v(\omega)$ and attenuation $\alpha(\omega)$, from the measurements (recall Eqs. (16a)–(16b)), a dedicated signal processing has been applied as in Gattin et al. [28]. In short, the signals recorded on the 32 elements of the receiving array were first averaged in order to filter out eventual spurious signals belonging to non-plane wave components and improve the SNR. To serve as an example, the resulting averaged signals $u_i(t)$ are depicted in Fig. 8(a)–(b) for a single measurement performed on the 1D-periodic sample with $N = 12$. Second, to isolate the echoes of interest, a tapered cosine window (*i.e.*, a Tukey window with a tapered fraction of 50%) of time length equal to 15 µs was applied to each signal $u_i(t)$. Third, a

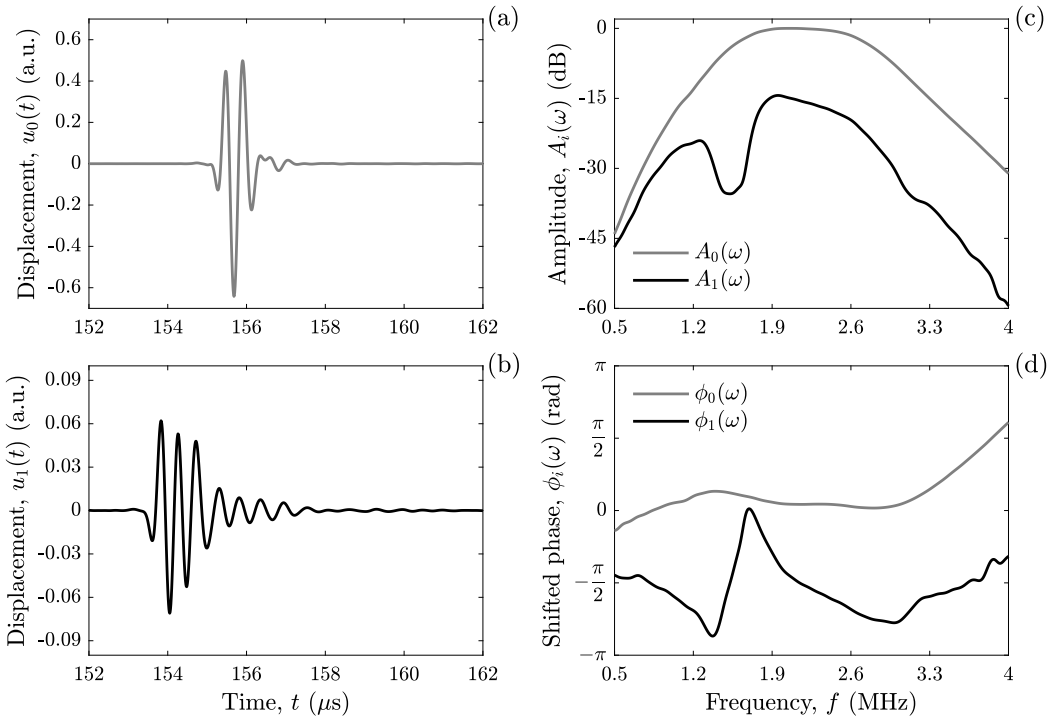

Fig. 8. Overview of typical signals recorded on a 1D-periodic sample ($N = 12$) using the insertion/substitution method: (a) Averaged time-domain signal $u_0(t)$ transmitted through water only; (b) Averaged time-domain signal $u_1(t)$ transmitted through the sample; (c) Amplitude $A_i(\omega)$ and (d) shifted phase spectra $\phi_i(\omega)$ extracted from both time-domain signals $u_i(t)$.

discrete Fourier transform was applied to the resulting signals over the total acquisition time to extract their amplitude $A_i(\omega)$ (see Fig. 8(c)) and phase spectra $\varphi_i(\omega)$. To remove the inherent 2π-ambiguity of conventional phase unwrapping algorithm [41,43], the latter were finally split as $\varphi_i(\omega) = \omega t_i + \phi_i(\omega)$, where ωt_i is the linear part of the phase spectra and $\phi_i(\omega)$ represent the phase variations (see Fig. 8(d)). As can be observed, compared to the signal $u_0(t)$ transmitted through water only (see Fig. 8(a)), the signal $u_1(t)$ transmitted through the 1D-periodic sample is strongly attenuated and exhibits a coda due to Bragg scattering (see Fig. 8(b)). In the Fourier domain, the latter turn to a sudden amplitude drop and an almost complete phase inversion between around 1.2 and 1.9 MHz (see Fig. 8(c)–(d)).

3.4. Measurement uncertainty

The measurement uncertainty was derived following the recommendations of the guide to the expression of uncertainty in measurement [44]. As only one sample of each kind was 3D-printed here, the measurement uncertainty only accounts for the uncertainty of the measurement method, that is the expanded uncertainty on the measured ultrasound characteristics (*i.e.*, the apparent phase velocity $v(\omega)$ and attenuation $\alpha(\omega)$), as a function of all potential sources of uncertainty on the input quantities. Towards this goal, the measurement uncertainty was here estimated by modeling the standard uncertainty on each input quantity as a Gaussian probability distribution [44]. Since the phase difference $\Delta\varphi(\omega)$ and amplitude ratio $A_0(\omega)/A_1(\omega)$, together with the sample dimensions and mass, resulted from independent observations, their respective standard uncertainties were assessed using Type A evaluation of standard uncertainty. Conversely, as the uncertainty of the water celerity mainly depends on the temperature and thereby on the resolution of the digital thermometer, its standard uncertainty was therefore assessed using Type B evaluation of standard uncertainty. The combined standard uncertainty on the measured ultrasound characteristics, denoted by $u_c(v(\omega))$ and $u_c(\alpha(\omega))$, was then evaluated by applying the law of propagation of uncertainty for uncorrelated input quantities to Eqs. (16a)–(16b), which results in

$$u_c(v(\omega)) = v^2(\omega)\sqrt{\left(\frac{u(c_w)}{c_w^2}\right)^2 + \left(\frac{u(\Delta\varphi(\omega))}{\omega h}\right)^2 + \left(\frac{\Delta\varphi^2(\omega)u(h)}{\omega h^2}\right)^2}, \tag{17a}$$

$$u_c(\alpha(\omega)) = \sqrt{\alpha^2(\omega)\left(\frac{u(h)}{h}\right)^2 + \frac{1}{h^2}\left(\frac{u(A_0(\omega)/A_1(\omega))}{A_0(\omega)/A_1(\omega)}\right)^2 + \frac{1}{h^2}\left(\frac{u_c(T_{\text{tot}}(\omega))}{T_{\text{tot}}(\omega)}\right)^2}, \tag{17b}$$

where $u(\cdot)$ denotes the standard uncertainty on the input quantities. In the same way, $u_c(T_{\text{tot}}(\omega))$ is the combined standard uncertainty of the total transmission coefficient, which has been deduced beforehand from Eq. (14). Likewise, the latter requires the prior calculation of the combined standard uncertainty of the mass density $u_c(\rho)$, which results from the measurements of the sample dimensions and mass. Finally, all uncertainties reported in the following for the measured ultrasound characteristics correspond to expanded uncertainties, denoted by $\pm U(v(\omega))$ and $\pm U(\alpha(\omega))$, given with a 95% confidence level (*i.e.*, using a coverage factor $k = 1.96$). It should be noted that the water density ρ_w was set equal to 998 kg/m^3 and not accounted for in the expression of uncertainty.

4. Experimental results

4.1. Model calibration

To evaluate the ability of the proposed modeling approaches to predict the periodic, viscoelastic behavior of the investigated samples, we first have to calibrate the mechanical properties of the constituent materials, *i.e.*, $k_m(\omega)$ and ρ_m (recall Eqs. (1) and (9)). These can be retrieved from the measurements performed on the two homogeneous

Table 1
Optimal model parameters $\hat{\boldsymbol{\theta}}_m$ identified from the measurements performed on the homogeneous VW$^+$ and TB$^+$ samples using Szabo's model. Their respective mass densities ρ_m were obtained by mass and volume measurements.

	Optimal model parameters $\hat{\boldsymbol{\theta}}_m$				Mass density
	$\hat{v}_{cm}$ m/s	$\hat{\alpha}_{cm}$ dB/cm	$\hat{y}_m$ –	$\hat{\alpha}_{0m}$ dB/cm	ρ_m kg/m^3
VW$^+$	2422.5	8.67	1.005	−0.85	1177.0
TB$^+$	1809.4	30.15	0.966	−0.78	1104.2

samples (*i.e.*, VW$^+$ and TB$^+$), which are achieved based on the measurement method described in Section 3.1. Towards this goal, we propose an optimization procedure to identify, for each constituent material $m \in \{\text{VW}^+, \text{TB}^+\}$, the four model parameters $\boldsymbol{\theta}_m = [v_{cm}, \alpha_{cm}, y_m, \alpha_{0m}]$ that minimize the following objective function $F(\boldsymbol{\theta}_m)$ in a least squares sense as in Gattin et al. [28],

$$F(\boldsymbol{\theta}_m) = \sqrt{\frac{1}{I}\sum_{i=1}^{I}\left|\frac{k_m(\omega_i) - k_m(\omega_i, \boldsymbol{\theta}_m)}{k_m(\omega_i)}\right|^2}, \tag{18}$$

where $k_m(\omega_i) = \omega_i / v_m(\omega_i) - j\alpha_m(\omega_i)$ and $k_m(\omega_i, \boldsymbol{\theta})$ are the measured and modeled complex wave numbers at the ith discrete frequency, which are respectively determined using Eqs. (16a)–(16b) and Eqs. (2)–(3). The variable I denotes the total number of discrete frequencies of the useful bandwidth on which the optimization is performed (from 1 to 4 MHz). The minimization of $F(\boldsymbol{\theta}_m)$ was carried out using the unconstrained Simplex algorithm [45]. The resulting optimal model parameters $\hat{\boldsymbol{\theta}}_m$, along with their respective mass densities ρ_m, are summarized in Table 1.

The matching between the measured ultrasound characteristics and the corresponding Szabo model outcomes calculated using the optimal model parameter $\hat{\boldsymbol{\theta}}_m$ is depicted in Fig. 9. As can observed, the measured ultrasound characteristics (continuous black lines) are satisfactorily captured by Szabo's model (dashed red lines) over the explored frequency range. The pseudo-R^2, calculated as recommended by Kvålseth [46] for a nonlinear regression analysis, are systematically higher than 0.98 for both the phase velocity $v_m(\omega)$ and attenuation $\alpha_m(\omega)$. Moreover, both constituent materials obey a quasi-linear power-law attenuation. Altogether, the model calibration results confirm previously observed evidences [27,28,47,48], and therefore allow us being confident in using these properties to feed the 1D-periodic models.

4.2. Model validation

The goal of this section is to compare the apparent ultrasound characteristics, *i.e.*, the phase velocity $v(\omega)$ and attenuation $\alpha(\omega)$, measured on the three 1D-periodic AM samples with those predicted by the mechanical models presented in Section 2. To this end, the model calibration results reported in Table 1 were used to feed the relations resulting from both the Bloch–Floquet analysis and the transfer matrix formalism (recall Eq. (1) and Eqs. (12a)–(12b), respectively). At this stage, it is worth mentioning that neither Bloch–Floquet analysis nor the transfer matrix formalism does account for the boundary conditions with the surrounding medium. However, in practice, it can be shown that the contribution of the latter becomes insignificant for a sufficiently large number of unit cells (see Supplementary Material 2), in which case the effects of periodicity are widely predominant.

Fig. 10 depicts the measured (continuous black lines) and modeled ultrasound characteristics for the three 1D-periodic samples with varying unit cell thicknesses d (but with constant total thickness $h = Nd$), where the latter have been obtained using both the Bloch–Floquet analysis (continuous red lines) and the transfer matrix formalism (dashed green lines). To serve as a further comparison, the ultrasound characteristics delivered by the effective model (dashed blue lines) are provided as well (recall Supplementary Materials 1). As can be observed, the apparent ultrasound characteristics predicted by both the Bloch–Floquet analysis and the transfer matrix formalism are overall in good agreement with their measured counterparts over the explored frequency range, as they nearly always fall within the 95% limits of agreement, as defined by the expanded uncertainties (gray areas). This thereby confirms that viscoelastic and periodic effects, *i.e.*, the slow and sudden dispersive variations discussed in Section 2.1, are properly accounted for in the modeling, no matter the designed unit cell thickness d. Moreover, as already observed in Fig. 6, Bloch–Floquet analysis slightly overestimates the apparent phase velocity and attenuation peaks compared to the transfer matrix formalism, especially for the samples with a low number of unit cells N, for which the finite size nature plays an important role.

In particular, it can first be observed that, as the unit cell thickness d increases (from panels (a) to (c)), the bandgap positions shift towards lower frequencies, and likewise the bandgaps become narrower and closer to each other on the explored frequency band. Second, it is noteworthy that the acoustic behavior of the sample with the lowest unit cell thickness d (see Fig. 10(a)) is also accurately captured by the effective model (dotted blue lines) below 1.5 MHz, as the corresponding wavelength is large compared to the unit cell thickness ($\lambda/d \approx 4$), thereby hindering periodicity effects to have a significant impact in this low frequency range. In addition, for this case the mismatch between the measured ultrasound characteristics and those predicted by the transfer matrix formalism becomes important above 2.8 MHz. This is due to the presence of a large bandgap close to the upper limit of the useful frequency bandwidth, which results in a sudden amplitude drop and phase inversion in the range of about 2.8–3.4 MHz. These effects altogether lead to measurements with a poor SNR (< −60 dB) in this frequency range, which explains the mismatch for the apparent attenuation $\alpha(\omega)$ there. These effects furthermore cause a failure of the phase reconstruction algorithm at higher frequencies too, thereby hampering an accurate recovery of the apparent phase velocity $v(\omega)$ above 2.8 MHz. Third, for the two samples with larger unit cell thickness d (see Fig. 10(b)–(c)), the transfer matrix formalism accurately predicts the experimentally observed dispersion, along with the positions and widths of the bandgaps, over a wide frequency band. The slight mismatch in the position and amplitude of secondary

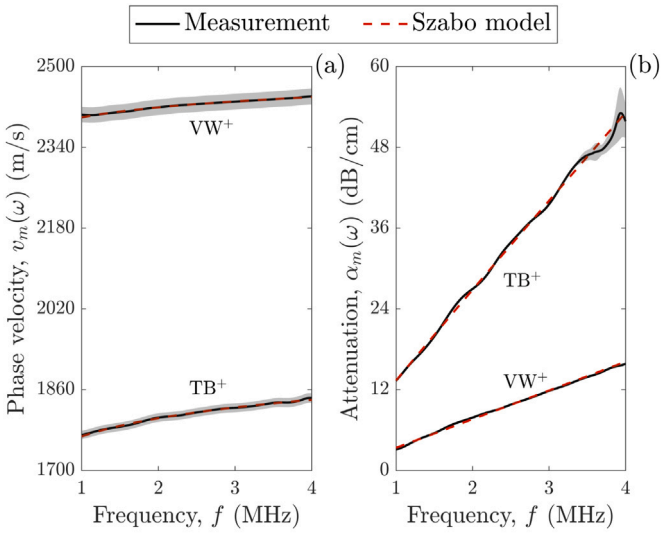

Fig. 9. Optimal matching between the measured ultrasound characteristics (continuous black lines) and the Szabo model outcomes (dashed red lines) calculated using the optimal model parameters $\hat{\boldsymbol{\theta}}_m$ for the homogeneous samples: (a) Phase velocity $v_m(\omega)$ and (b) Attenuation $\alpha_m(\omega)$, with $m \in \{\text{VW}^+, \text{TB}^+\}$. The gray areas display the expanded uncertainties on the experimental results.

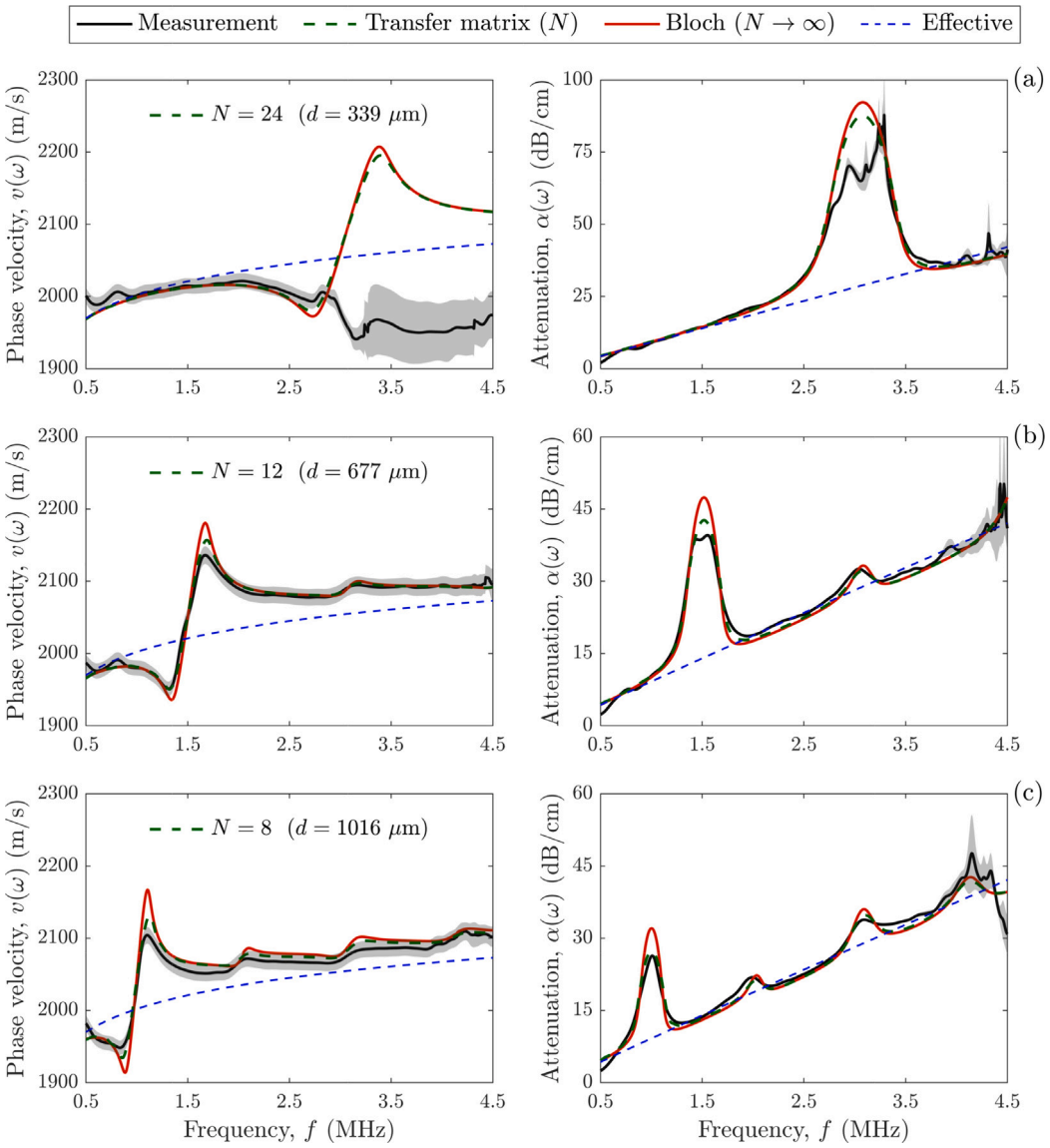

Fig. 10. Comparison between the measured and modeled apparent ultrasound characteristics, *i.e.*, phase velocity $v(\omega)$ and attenuation $\alpha(\omega)$, for the three 1D-periodic AM samples with varying unit cell numbers and thicknesses: (a) $N = 24$ ($d = 339$ μm); (b) $N = 12$ ($d = 677$ μm), and (c) $N = 8$ ($d = 1016$ μm). The gray areas display the expanded uncertainties on the experimental results.

bandgaps, especially visible for the attenuation $\alpha(\omega)$, is likely to be due to sample imperfections (*e.g.*, fluctuations of the period d). This point will be further discussed in Section 5.

5. Discussion

In this study, we introduced two different approaches for modeling longitudinal ultrasound wave propagation across a 1D-periodic biphasic medium made of viscoelastic constituent materials. First, Bloch–Floquet analysis has been discussed in the frame of viscoelasticity and compared with the classical elastic case, with the aim of identifying the relative contributions of both viscoelasticity and periodicity on the apparent ultrasound characteristics of interest (*i.e.*, complex wave number, phase velocity, and attenuation). Second, since Bloch–Floquet analysis relies on the assumption of an infinite number of periodic spatial repetitions of the unit cell, the impact of the finite size nature of the medium has been assessed by making use of the transfer matrix formalism. In order to support the modeling results, both homogeneous and 1D-periodic samples have been additively manufactured using a multimaterial 3D printing technology, which allowed for a local control of the spatial arrangement of two phases with dissimilar properties (*i.e.*, a rigid glassy polymer and an elastomeric polymer). All samples have then been measured in through-transmission using multielement probes driven by a multichannel electronics. The measurements performed on the homogeneous samples were processed to retrieve the phase velocity and attenuation of the constituent materials, which were in turn used to feed both periodic models. The latter were subsequently compared to the measurements performed on the 1D-periodic samples for validation purposes.

The main findings were as follows: first, the modeling results, along with their confrontation to the measurements, altogether suggest that it is essential to account for viscoelasticity to predict the complex acoustic behavior (*i.e.*, apparent dispersion, attenuation, bandgaps) of periodic media made of photopolymer-based AM materials in the MHz regime. Indeed, the latter results from the coupling of two contributions – the constitutive relation of the constituent materials plus their spatial arrangement –, which cannot be captured by more simplistic models based on the purely elastic periodic model or effective medium theory. Second, the critical assessment of the differences between the two proposed modeling approaches showed that Bloch–Floquet analysis tends to overestimate the apparent ultrasound characteristics in

the bandgaps, especially in the case of finite size media with a low number of unit cell repetitions. Nevertheless, we showed that the associated results converge towards those obtained with the transfer matrix formalism when considering a sufficiently large number of unit cell repetitions. As a by-product, it is noteworthy that polyjet AM has been shown to allow for the design of periodic multi-material samples exhibiting bandgaps in the MHz regime. This constitutes an achievement in itself, since only a few studies have experimentally evidenced ultrasonic bandgaps in this frequency regime using bulk waves [17,21]. In addition, the proposed approach not only exploits the amplitude of the signal but also its phase, which altogether allow recovering apparent ultrasound characteristics, and thereby the dispersion relation, while most studies focusing on ultrasonic bandgaps only have exploited the measurements of reflection and transmission coefficients so far [19].

Despite these promising results, our study suffers from some limitations. First, the expanded measurement uncertainty was not always sufficient to explain the slight deviations from the model predictions (noticeable in particular in the position and amplitude of secondary bandgaps in Fig. 10). In this regard, several sources of uncertainty are believed to impact the modeling predictions as well. Among these, it is worth mentioning the inevitable sample imperfections, which may result from the manufacturing process. For instance, the three 1D-periodic samples were designed and modeled to have perfectly identical unit cells, no matter their thickness d and numbers N, with a volume fraction for each constituent material equal to 50% (*i.e.*, $d_A = d_B = d/2$). Nevertheless, uncertainties on the volume fraction and on the intra-sample variability of the unit cell thickness could lead to a certain fluctuation of the periodicity, whose impact was not accounted for in the comparison between the model predictions and the experimental data. Likewise, it has also been shown that this printing technology may lead to a gradient of properties at the interfaces between the two photopolymers [49], as the latter can blend to some extent before curing occurs. Such a gradient, whose expected width in the current printing setting is about 50 μm, could reduce the apparent impedance contrast between the two photopolymers, and therefore mitigate the impact of periodicity. Altogether, the quantitative assessment of these effects is difficult and beyond the scope of this study, as it would require the application of minimally invasive and long-winded experimental methods, such as nanoindentation. Second, this study deliberately focused on the simplistic case of longitudinal wave propagation across 1D-periodic media only, as it offers a well-controlled framework to disentangle the relative contributions of viscoelasticity and periodicity, as well as to compare modeling approaches capable of accounting for these phenomena. The extension to more complex architectures involving 2D or even 3D-periodicity, together with potential mode conversion, requires some modeling considerations. For instance, in such cases the dispersion relation resulting from Bloch–Floquet analysis (recall Eq. (1)) can no longer be solved analytically, and one therefore has to turn to numerical approaches, for which the consideration of viscoelasticity is not necessarily trivial [50–52]. Conversely, although the transfer matrix formalism can be extended to account for 2D propagation in oblique incidence [53], it is not appropriate anymore for higher order spatial periodicity, and time-transient simulations by means of the finite element or finite difference methods should be used instead [54], at the expense of a higher computational cost. Third, the current experimental configuration was limited to the exploitation of through-transmitted signals so far. However, many applications in ultrasonic nondestructive testing require measurements to be achieved in reflection, since the back side of the investigated sample is not always accessible. In that sense, the transfer matrix formalism has the advantage of naturally providing the reflection coefficient (in amplitude and phase) as a way to retrieve complementary information on viscoelasticity and periodicity, while such configuration is difficult to figure out using Bloch–Floquet analysis.

Altogether, these limitations make the ultrasound characterization of periodic media a challenging problem with much potential for future works. As a next step, we will experimentally and numerically investigate more complex architectures by tailoring the spatial arrangement of the two elementary constituents (*e.g.*, squared inclusions, gyroids) to achieve programmable acoustic behaviors. Given that photopolymer-based AM is experiencing a wide dissemination, this research will not only be valuable to conduct fundamental studies on ultrasonic bandgaps in 3D-printed periodic media [21], but also to develop accurate monitoring techniques towards the characterization of scaffolds for tissue engineering applications [14].

Declaration of competing interest

The authors declare that they have no known competing financial interests or personal relationships that could have appeared to influence the work reported in this paper.

Data availability

The authors do not have permission to share data.

Acknowledgments

This work was partially supported by the “Bonus Qualité Recherche” for young researchers (Faculté des Sciences et Technologie, Université Paris-Est Créteil, France).

Appendix A. Supplementary data

Supplementary materials related to the effective medium theory and the impact of the boundary conditions mentioned in this article can be found online at https://doi.org/10.1016/j.ultras.2023.106951.

References

[1] C.J. Naify, K.H. Matlack, M.R. Haberman, Introduction to the special issue on additive manufacturing and acoustics, J. Acoust. Soc. Am. 151 (1) (2022) 387–389.
[2] A.J. Cloonan, D. Shahmirzadi, R.X. Li, B.J. Doyle, E.E. Konofagou, T.M. McGloughlin, 3D-printed tissue-mimicking phantoms for medical imaging and computational validation applications, 3D Print. Addit. Manuf. 1 (1) (2014) 14–23.
[3] J.-R. Jacquet, F. Ossant, F. Levassort, J.-M. Grégoire, 3-D-printed phantom fabricated by photopolymer jetting technology for high-frequency ultrasound imaging, IEEE Trans. Ultrason. Ferroelectr. Freq. Control 65 (6) (2018) 1048–1055.
[4] G. Maimbourg, A. Houdouin, T. Deffieux, M. Tanter, J.-F. Aubry, 3D-printed adaptive acoustic lens as a disruptive technology for transcranial ultrasound therapy using single-element transducers, Phys. Med. Biol. 63 (2) (2018) 025026.
[5] M. Ferri, J.M. Bravo, J. Redondo, S. Jiménez-Gambín, N. Jiménez, F. Camarena, J.V. Sánchez-Pérez, On the evaluation of the suitability of the materials used to 3D print holographic acoustic lenses to correct transcranial focused ultrasound aberrations, Polymers 11 (9) (2019) 1521.
[6] M. Askari, D.A. Hutchins, P.J. Thomas, L. Astolfi, R.L. Watson, M. Abdi, M. Ricci, S. Laureti, L. Nie, S. Freear, et al., Additive manufacturing of metamaterials: A review, Addit. Manuf. 36 (2020) 101562.
[7] L. D’Alessandro, E. Belloni, R. Ardito, A. Corigliano, F. Braghin, Modeling and experimental verification of an ultra-wide bandgap in 3D phononic crystal, Appl. Phys. Lett. 109 (22) (2016) 221907.
[8] K.H. Matlack, A. Bauhofer, S. Krödel, A. Palermo, C. Daraio, Composite 3D-printed metastructures for low-frequency and broadband vibration absorption, Proc. Natl. Acad. Sci. 113 (30) (2016) 8386–8390.
[9] C.W. Cushing, M.J. Kelsten, X. Su, P.S. Wilson, M.R. Haberman, A.N. Norris, Design and characterization of a three-dimensional anisotropic additively manufactured pentamode material, J. Acoust. Soc. Am. 151 (1) (2022) 168–179.
[10] L. Ribeiro, V. Dal Poggetto, B. Huallpa, J. Arruda, Bloch wavenumber identification of periodic structures using Prony’s method, Mech. Syst. Signal Process. 178 (2022) 109242.
[11] M. Oudich, N.J. Gerard, Y. Deng, Y. Jing, Bandgap engineering in phononic crystals and elastic metamaterials, arXiv preprint https://arxiv.org/abs/2207.05234.
[12] P. Fratzl, R. Weinkamer, Nature’s hierarchical materials, Prog. Mater. Sci. 52 (8) (2007) 1263–1334.

[13] R. Seidel, A. Roschger, L. Li, J.J. Bizzarro, Q. Zhang, J. Yin, T. Yang, J.C. Weaver, P. Fratzl, P. Roschger, et al., Mechanical properties of stingray tesserae: high-resolution correlative analysis of mineral density and indentation moduli in tessellated cartilage, Acta Biomater. 96 (2019) 421–435.
[14] M. Aliabouzar, G.L. Zhang, K. Sarkar, Acoustic and mechanical characterization of 3D-printed scaffolds for tissue engineering applications, Biomed. Mater. 13 (5) (2018) 055013.
[15] C. Sun, E. Dong, J. Chen, J. Zheng, J. Kang, Z. Jin, C. Liu, L. Wang, D. Li, The promotion of mechanical properties by bone ingrowth in additive-manufactured titanium scaffolds, J. Funct. Biomater. 13 (3) (2022) 127.
[16] A.A. Zadpoor, Meta-biomaterials, Biomater. Sci. 8 (1) (2020) 18–38.
[17] M. Torres, F.M. de Espinosa, Ultrasonic band gaps and negative refraction, Ultrasonics 42 (1–9) (2004) 787–790.
[18] O. Lenoir, P. Maréchal, Study of plane periodic multilayered viscoelastic media: Experiment and simulation, in: IEEE Int. Ultrason. Symp., 2009, pp. 1028–1031.
[19] P. Maréchal, O. Lenoir, A. Khaled, M. Ech Cherif El Kettani, D. Chenouni, Viscoelasticity effect on a periodic plane medium immersed in water, Acta Acust. United Ac. 100 (6) (2014) 1036–1043.
[20] E.J. Smith, K.H. Matlack, Metal additively manufactured phononic materials as ultrasonic filters in nonlinear ultrasound measurements, J. Acoust. Soc. Am. 149 (6) (2021) 3739–3750.
[21] A. Kruisová, M. Švčík, H. Seiner, P. Sedlák, B. Román-Manso, P. Miranzo, M. Belmonte, M. Landa, Ultrasonic bandgaps in 3D-printed periodic ceramic microlattices, Ultrasonics 82 (2018) 91–100.
[22] F. Lucklum, M. Vellekoop, Rapid prototyping of 3D phononic crystals using high-resolution stereolithography fabrication, Proc. Eng. 120 (2015) 1095–1098.
[23] J.A. Iglesias Martínez, J. Moughames, G. Ulliac, M. Kadic, V. Laude, Three-dimensional phononic crystal with ultra-wide bandgap at megahertz frequencies, Appl. Phys. Lett. 118 (6) (2021) 063507.
[24] L. Zorzetto, D. Ruffoni, Wood-inspired 3D-printed helical composites with tunable and enhanced mechanical performance, Adv. Funct. Mater. 29 (1) (2019) 1805888.
[25] M.J. Mirzaali, M. Cruz Saldívar, A. Herranz de la Nava, D. Gunashekar, M. Nouri-Goushki, E.L. Doubrovski, A.A. Zadpoor, Multi-material 3D printing of functionally graded hierarchical soft–hard composites, Adv. Eng. Mater. 22 (7) (2020a) 1901142.
[26] M. Mirzaali, A.H. De La Nava, D. Gunashekar, M. Nouri-Goushki, R. Veeger, Q. Grossman, L. Angeloni, M. Ghatkesar, L. Fratila-Apachitei, D. Ruffoni, E.L. Doubrovski, A.A. Zadpoor, Mechanics of bioinspired functionally graded soft-hard composites made by multi-material 3D printing, Compos. Struct. 237 (2020b) 111867.
[27] A. Aghaei, N. Bochud, G. Rosi, Q. Grossman, D. Ruffoni, S. Naili, Ultrasound characterization of bioinspired functionally graded soft-to-hard composites: Experiment and modeling, J. Acoust. Soc. Am. 151 (3) (2022) 1490–1501.
[28] M. Gattin, N. Bochud, G. Rosi, Q. Grossman, D. Ruffoni, S. Naili, Ultrasound characterization of the viscoelastic properties of additively manufactured photopolymer materials, J. Acoust. Soc. Am. 152 (3) (2022) 1901–1912.
[29] M. Rousseau, Floquet wave properties in a periodically layered medium, J. Acoust. Soc. Am. 86 (6) (1989) 2369–2376.
[30] A. Khaled, P. Maréchal, O. Lenoir, M.E.-C. El-Kettani, D. Chenouni, Study of the resonances of periodic plane media immersed in water: Theory and experiment, Ultrasonics 53 (3) (2013) 642–647.
[31] T.L. Szabo, Causal theories and data for acoustic attenuation obeying a frequency power law, J. Acoust. Soc. Am. 97 (1) (1995) 14–24.
[32] T.L. Szabo, J. Wu, A model for longitudinal and shear wave propagation in viscoelastic media, J. Acoust. Soc. Am. 107 (5) (2000) 2437–2446.
[33] M. O'Donnell, E. Jaynes, J. Miller, Kramers–Kronig relationship between ultrasonic attenuation and phase velocity, J. Acoust. Soc. Am. 69 (3) (1981) 696–701.
[34] J.P. Hollkamp, M. Sen, F. Semperlotti, Analysis of dispersion and propagation properties in a periodic rod using a space-fractional wave equation, J. Sound Vib. 441 (2019) 204–220.
[35] J. White, F. Angona, Elastic wave velocities in laminated media, J. Acoust. Soc. Am. 27 (2) (1955) 310–317.
[36] N. Bochud, A. Gomez, G. Rus, A. Peinado, A sparse digital signal model for ultrasonic nondestructive evaluation of layered materials, Ultrasonics 62 (2015) 160–173.
[37] N. Cretu, G. Nita, Pulse propagation in finite elastic inhomogeneous media, Comput. Mater. Sci. 31 (3–4) (2004) 329–336.
[38] A. Dell, A. Krynkin, K. Horoshenkov, The use of the transfer matrix method to predict the effective fluid properties of acoustical systems, Appl. Acoust. 182 (2021) 108259.
[39] J.J. Kaufman, W. Xu, A.E. Chiabrera, R.S. Siffert, Diffraction effects in insertion mode estimation of ultrasonic group velocity, IEEE Trans. Ultrason. Ferroelectr. Freq. Control 42 (2) (1995) 232–242.
[40] J. Bustillo, J. Fortineau, G. Gautier, M. Lethiecq, Ultrasonic characterization of porous silicon using a genetic algorithm to solve the inverse problem, NDT & E Int. 62 (2014) 93–98.
[41] P. He, J. Zheng, Acoustic dispersion and attenuation measurement using both transmitted and reflected pulses, Ultrasonics 39 (1) (2001) 27–32.
[42] W. Marczak, Water as a standard in the measurements of speed of sound in liquids, J. Acoust. Soc. Am. 102 (5) (1997) 2776–2779.
[43] J. Niemi, Y. Aitomäki, T. Löfqvist, Ultrasonic measurements and modelling of attenuation and phase velocity in pulp suspensions, in: IEEE Int. Ultrason. Symp. 2, 2005, pp. 775–779.
[44] BIPM, IEC, IFCC, ILAC, ISO, IUPAC, IUPAP, OIML, Evaluation of measurement data – guide to the expression of uncertainty in measurement, in: Joint Committee for Guides in Metrology, JCGM, Vol. 100, 2008, pp. 1–116.
[45] J.A. Nelder, R. Mead, A simplex method for function minimization, Comput. J. 7 (4) (1965) 308–313.
[46] T.O. Kvålseth, Cautionary note about R^2, Am. Stat. 39 (4) (1985) 279–285.
[47] M.D. Farinas, T. Álvarez-Arenas, G. Cummins, M.P.Y. Desmulliez, V. Seetohul, S. Cochran, Assessment of the ultrasonic properties of additive manufactured materials for passive components of piezoelectric transducers, in: IEEE Int. Ultrason. Symp., 2016, pp. 1–4.
[48] M. Bakaric, P. Miloro, A. Javaherian, B.T. Cox, B.E. Treeby, M.D. Brown, Measurement of the ultrasound attenuation and dispersion in 3D-printed photopolymer materials from 1 to 3.5 MHz, J. Acoust. Soc. Am. 150 (4) (2021) 2798–2805.
[49] L. Zorzetto, L. Andena, F. Briatico-Vangosa, L. De Noni, J.-M. Thomassin, C. Jérôme, Q. Grossman, A. Mertens, R. Weinkamer, M. Rink, et al., Properties and role of interfaces in multimaterial 3D printed composites, Sci. Rep. 10 (1) (2020) 1–17.
[50] M.I. Hussein, Theory of damped Bloch waves in elastic media, Phys. Rev. B 80 (21) (2009) 212301.
[51] M. Collet, M. Ouisse, M. Ruzzene, M. Ichchou, Floquet–Bloch decomposition for the computation of dispersion of two-dimensional periodic, damped mechanical systems, Int. J. Solids Struct. 48 (20) (2011) 2837–2848.
[52] D. Faraci, C. Comi, J.-J. Marigo, Band gaps in metamaterial plates: Asymptotic homogenization and Bloch-Floquet Approaches, J. Elasticity 148 (1) (2022) 55–79.
[53] M.J. Lowe, Matrix techniques for modeling ultrasonic waves in multilayered media, IEEE Trans. Ultrason. Ferroelectr. Freq. Control. 42 (4) (1995) 525–542.
[54] G. Aguzzi, C. Kanellopoulos, R. Wiltshaw, R.V. Craster, E.N. Chatzi, A. Colombi, Octet lattice-based plate for elastic wave control, Sci. Rep. 12 (1) (2022) 1–14.